arXiv:cond-mat/0601107v1 [cond-mat.mtrl-sci] 5 Jan 2006

Dynamics of Bulk vs. Nanoscale WS_2: Local Strain and Charging Effects

R.D. Luttrell[1], S. Brown[1], J. Cao[1], J.L. Musfeldt[1], R. Rosentsveig[2], and R. Tenne[2]
[1]*Department of Chemistry, University of Tennessee, Knoxville, Tennessee, USA 37996 and*
[2]*Department of Materials and Interfaces, Weizmann Institute of Science, Rehovot, Israel 76100*

We measured the infrared vibrational properties of bulk and nanoparticle WS_2 in order to investigate the structure-property relations in these novel materials. In addition to the symmetry-breaking effects of local strain, nanoparticle curvature modifies the local charging environment of the bulk material. Performing a charge analysis on the *xy*-polarized E_{1u} vibrational mode, we find an approximate 1.5:1 intralayer charge difference between the layered 2H material and inorganic fullerene-like (IF) nanoparticles. This effective charge difference may impact the solid-state lubrication properties of nanoscale metal dichalcogenides.

PACS numbers: 63.22.+m, 78.20.Ci, 61.46.+w, 78.30.-j

I. INTRODUCTION

Inorganic fullerene-like (IF) nanostructures have recently attracted attention due to their unique closed cage structures and outstanding solid-state lubricating behavior [1, 2, 3]. Just as carbon fullerenes are nanoscale analogs of layered graphite, IF nanoparticles and nanotubes are curved analogs of the corresponding quasi-two-dimensional material. Layered and nanoscale metal dichalcogenides are prototypes in this regard, and the discovery of the WS_2-based family of IF nanoparticles (Fig. 1) provides the opportunity to investigate structure-property relations in bulk vs. nanoscale materials. At the same time, the IF materials hold out the potential for important applications. In addition to use in rechargeable batteries, optical devices, and in impact-resistant nanocomposities, extensive mechanical properties testing demonstrates that the friction coefficient of IF-WS_2 nanoparticles is reduced up to 50% compared with the 2H-WS_2 parent compound, maintaining excellent lubricating behavior even under very high loads, ultra-high vacuum, and in humid conditions [4, 5, 6, 7, 8, 9, 10]. Because of these observations, major efforts have been directed at understanding the connection between bulk and microscopic properties and exploiting the commercial promise of these novel nanomaterials.

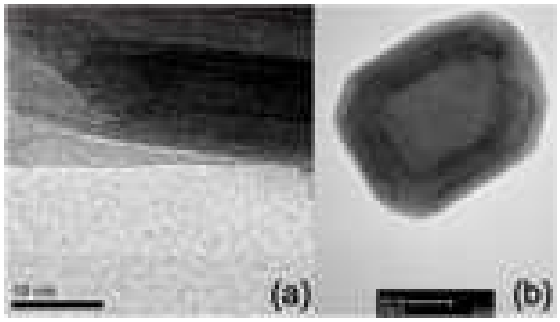


FIG. 1: Transmission electron microscope images of (a) layered 2H-WS_2 and (b) a representative IF-WS_2 nanoparticle (b). Each nanoparticle consists of a hollow core and several W-S-W layers. The average particle diameter is ∼120 - 200 nm for the materials of interest here. The IF nanoparticle shown here is slightly smaller than average.

2H-WS_2 belongs to the space group $P6_3/mmc$ (D^4_{6h}) and contains two formula units per unit cell [11]. The bonding is well-known to consist of strong covalent intralayer forces and weak van der Waals interactions between adjacent layers [12, 13]. Each MX_2 layer (M = group VIB metal, X = group VIA element) contains a layer of metal atoms, sandwiched between two chalcogen layers, with each metal atom bonded to six chalcogen atoms in a trigonal prismatic arrangement. A group theoretical analysis (Table A.1, Appendix) gives a total of 18 normal modes [14]. The doubly degenerate E_{1u} and singly degenerate A_{2u} vibrational modes are infrared active; the conjugate gerade modes are Raman active. Figure 2 displays the relevant displacement vectors. Note that the infrared active *xy*-polarized E_{1u} and *z*-polarized A_{2u} modes are associated with intralayer and interlayer motion, respectively. This directional selectivity provides a sensitive and microscopic probe of charge and bonding interactions that we will employ in this work to assess effective total and local charge differences between the bulk and nanoscale materials [15, 16, 17, 18, 19]. X-ray diffraction reveals that the local structure of 2H-WS_2 is preserved within the unit cell of an IF nanoparticle with the exception of a 2% lattice expansion along the *z*-axis [20, 21]. This lattice expansion is attributed to strain in the curved WS_2 layers [21, 22], each of which has a slightly different radius due to layer inhomogeneities (Fig. 1(b)). The lattice modes of 2H-WS_2 were previously investigated using combined Raman and inelastic neutron scattering, demonstrating that the two-phonon resonance Raman effects are second-order processes involving the longitudinal acoustic mode at the K point of the Brillouin zone [23]. Previous studies also indicate that the new Raman peaks in spectra of IF-WS_2 nanotubes and nanoparticles should be assigned as disorder-induced zone edge phonons [24]. More recent Raman

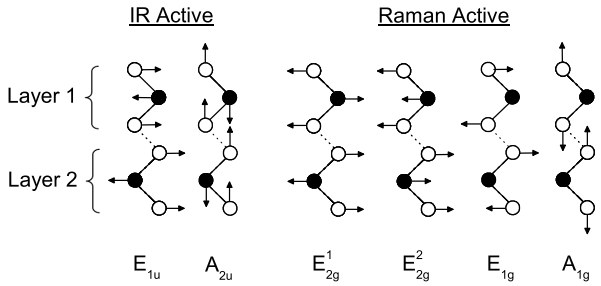


FIG. 2: Displacement vectors of the infrared and Raman active modes of 2H-WS_2. The dashed line between the two layers represents the weak van der Waals force.

work demonstrates that the 33 cm^{-1} E_{2g} shearing or "rigid layer" mode is almost completely blocked in IF-WS_2 due to surface strain hindering intralayer motion in the nanoparticles [25]. Extensive optical properties and STM work indicates that the indirect gap is smaller in the IF nanoparticles compared to that in the bulk [26, 27]. A and B exciton positions are also sensitive to confinement and the number of layers in the nanoparticle [24, 26].

In order to investigate structure-property relationships in these chemically identical but morphologically different metal dichalcogenides, we measured the infrared reflectance spectra of both 2H- and IF-WS_2 powders and performed a charge analysis to extract total and local effective charge from the oscillator parameters of the major infrared active phonon modes. We found an approximate 1.5:1 intralayer charge difference between the 2H- bulk and IF-nanoparticle materials, respectively. The trend is different in the interlayer direction, reflecting a slightly enhanced z interaction in the nanoparticles. We discuss how differences in both charge and strain may be connected to the macroscopic properties of these materials.

II. EXPERIMENTAL METHODS

IF-WS_2 was prepared from its oxide precursor, WO_3, following previously published procedures [1, 21, 28, 29, 30, 31, 32]. The IF nanoparticles of interest in this work range in size from ∼120 - 200 nm in diameter. The particle size, shape and distribution have been studied by x-ray powder diffraction [21], scanning tunneling microscopy [27], and high-resolution transmission electron microscopy [21, 27, 28]. Pressed isotropic pellets were prepared to investigate the dynamical properties. Bulk 2H-WS_2 was also measured for comparison (Alfa Aesar, 99.8%).

Near-normal infrared reflectance was measured over a wide frequency range using a series of spectrometers including a Bruker 113V Fourier transform infrared spectrometer, an Equinox 55 Fourier transform instrument (equipped with a microscope attachment), and a Perkin

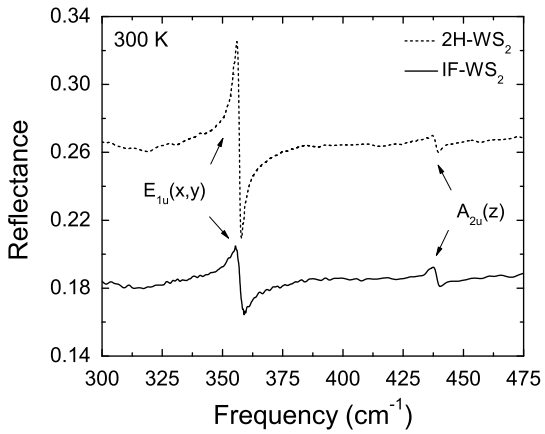


FIG. 3: 300 K reflectance spectra of 2H- and IF-WS_2. The E_{1u} and A_{2u} modes are infrared active in these materials, with xy- and z-directed polarizations, respectively.

Elmer Lambda 900 grating spectrometer, covering the frequency range from 25 - 52000 cm^{-1}. A helium-cooled bolometer detector was employed in the far-infrared for added sensitivity. Both 0.5 and 2 cm^{-1} resolution were used in the infrared, whereas 3 nm resolution was used in the optical regime. Variable temperature measurements were carried out with a continuous-flow helium cryostat and temperature controller. A Kramers-Kronig analysis was used to calculate the optical constants from the measured reflectance, yielding information on the dispersive and lossy response of each material [33, 34]. Standard peak-fitting techniques were employed, where appropriate.

III. RESULTS AND DISCUSSION

A. Understanding Charge Localization Effects in 2H- and IF-WS_2

Figure 3 displays a close-up view of the far infrared reflectance spectra of 2H- and IF-WS_2 at 300 K. We assign the major features in the reflectance (at 356 and 437 cm^{-1}) as the E_{1u} and A_{2u} modes, respectively [14, 35]. These modes are strikingly different in the two materials. The E_{1u} mode appears damped and suppressed in IF-WS_2 compared to the 2H- analog, whereas the A_{2u} mode is slightly more pronounced in the IF compound compared to that in the bulk. These differences can be quantified using traditional dielectric oscillator models and fitting techniques which, in combination with appropriate models, allow us to assess the charge characteristics of the nanomaterial as compared to the bulk.

One well-established approach for quantifying charge in a material involves assessment of both total and local effective charge [15, 16, 17, 18, 19]. As discussed by

TABLE I:
Classical Oscillator Parameters and Optical Phonon Frequencies for 2H- and IF-WS_2

	E_{1u} Mode		A_{2u} Mode	
300 K	2H-WS_2	IF-WS_2	2H-WS_2	IF-WS_2
Oscillator strength, S	0.031	0.014	0.002	0.002
Damping constant, γ	0.005	0.010	0.004	0.006
ω_{TO} (cm^{-1})	356.47	356.97	438.32	439.01
ω_{LO} (cm^{-1})	357.10	357.28		
ω_{LO}-ω_{TO} (cm^{-1})	0.63	0.31		
ϵ_∞	9.58	6.26		
10 K				
Oscillator strength, S	0.040	0.017	0.005	0.004
Damping constant, γ	0.004	0.010	0.006	0.004
ω_{TO} (cm^{-1})	358.30	358.61	440.80	440.87
ω_{LO} (cm^{-1})	359.14	359.20		
ω_{LO}-ω_{TO} (cm^{-1})	0.84	0.59		
ϵ_∞	8.92	6.46		

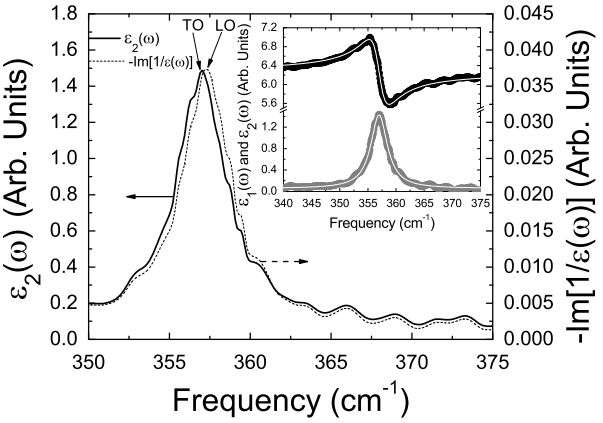


FIG. 4: Frequency dependence of the imaginary part of the dielectric function, $\epsilon_2(\omega)$, and the energy loss function, $-\mathrm{Im}(1/\epsilon(\omega))$, of IF-$WS_2$ at 300 K. Longitudinal optical (LO) and transverse optical (TO) frequencies are indicated. The inset displays an oscillator fit (white line) to the real (black) and imaginary (gray) parts of the dielectric function, $\epsilon_1(\omega)$, and $\epsilon_2(\omega)$, for IF-WS_2 at 300 K.

Burstein *et al.* [19], macroscopic effective charge, e_T^*, is a measure of the electric moment per unit cell and contains contributions from both the localized charge on the ion sites and the charge generated throughout the unit cell. Therefore, e_T^*, can be separated into a localized part, e_l^*, and a nonlocalized part, e_{nl}^*,

$$e_T^* = e_l^* + e_{nl}^*. \tag{1}$$

Here, e_l^* is defined as the localized moment generated per unit displacement of an ion. It induces a local field through dipole-dipole interactions which contributes to the reduction of the transverse optical (TO) phonon frequency. Although e_T^* can be a good measure of bond ionicity or covalency in layered MX_2 transition-metal dichalcogenides, e_l^* gives a more appropriate representation of bonding interactions because it quantifies charge on the ionic sites [15].

Total macroscopic effective charge, e_T^*, is given as

$$\frac{e_T^*}{e} = \frac{\omega_{TO} c}{e}\sqrt{\frac{4\pi^2\epsilon_0\bar{m}S}{N}}. \tag{2}$$

Here, ω_{TO} is the TO phonon frequency (in cm^{-1}), S is the oscillator strength, N is the number of WS_2 formula units per unit volume, $\bar{m}$ is the mode mass [36], e is the electronic charge, c is the speed of light (in cm/s), and ϵ_0 is the permittivity of free space. Note that for comparison of two similar materials, such as 2H- and IF-WS_2, oscillator strength and TO phonon frequency will be the distinguishing parameters. Localized effective charge [15], e_l^*, is determined as

$$\frac{e_l^*}{e} = c\sqrt{(\omega_{LO}^2 - \omega_{TO}^2)\frac{\bar{m}\epsilon_0}{e^2 LN}}. \tag{3}$$

Here, ω_{LO} is the longitudinal optical (LO) phonon frequency (in cm^{-1}) and L is the Lorentz factor for a hexagonal lattice [37]. Precise measurement of the LO-TO splitting is key to distinguishing local charge differences in 2H- and IF-WS_2.

In order to obtain the parameters needed to extract total effective and local charge for both 2H- and IF-WS_2, we carried out a Kramers-Kronig analysis of the measured reflectance. LO and TO phonon frequencies are obtained directly from the optical constants, for instance, as peaks in the energy loss function, $-\mathrm{Im}(1/\epsilon(\omega))$, and in the imaginary part of the frequency dependent dielectric function, $\epsilon_2(\omega)$, respectively. Figure 4 shows an example of these optical constants and the straightforward extraction of LO and TO phonon frequencies for IF-WS_2 at 300 K. Oscillator strength, S, is obtained by simultaneously fitting the real and imaginary parts of the complex dielectric function, $\tilde{\epsilon}(\omega) = \epsilon_1(\omega) + i\epsilon_2(\omega)$, using the three parameter model

$$\tilde{\epsilon}(\omega) = \epsilon_\infty + \sum_j \frac{S_j\omega_j^2}{\omega_j^2 - \omega^2 - i\gamma_j\omega_j\omega}. \tag{4}$$

Here, the subscript j refers to the mode of interest, γ is the damping constant, and ϵ_∞ is the high frequency dielectric constant [16, 18, 33, 38]. As an example, the inset of Fig. 4 shows an oscillator fit of the real and imaginary parts of the complex dielectric function for the E_{1u} mode of IF-WS_2 at 300 K. The classical oscillator parameters of both 2H- and IF-WS_2 are summarized in Table I. These parameters, along with Eqns. 2 and 3, allow us to evaluate the charge characteristics.

The small LO-TO splitting in both 2H- and IF-WS_2 indicates that the metal-chalcogen bond is highly covalent within the layer, in agreement with previous results for WS_2 as well as other well-known covalent compounds

TABLE II:
Macroscopic and Localized Effective Charge Values for 2H- and IF-WS_2

		E_{1u} Mode		A_{2u} Mode	
		2H-WS_2	IF-WS_2	2H-WS_2	IF-WS_2
300 K	e_T^*/e	0.45	0.30	0.15	0.16
	e_l^*/e	0.20	0.14		
10 K	e_T^*/e	0.51	0.34	0.22	0.20
	e_l^*/e	0.23	0.20		

[a] e_l^* cannot be obtained for the z-polarized interlayer A_{2u} mode due to the negative Lorentz factor [40].
[b] Error bars on the total and local charge values are ± 0.02.

including MoS_2, $MoSe_2$, and WSe_2 [15, 16, 17, 18, 19]. In contrast, Uchida and Tanaka report large LO-TO splittings for several group IV transition-metal dichalcogenides, including 1T-$TiSe_2$, 1T-$ZrSe_2$, and 1T-$HfSe_2$, which are considered to be highly ionic materials [15]. Physically, the smaller LO-TO splitting of the E_{1u} mode in IF-WS_2 (Table 1), indicates that the IF- nanoparticles are slightly more covalent than the parent 2H- compound. This result indicates that nanoparticle curvature changes the charge-sharing environment within the layer.

Table II displays the total macroscopic and local charge for both 2H- and IF-WS_2. Using the xy-polarized E_{1u} mode as a probe of charge within the layer, we find that $e_T^* = 0.45$ for 2H-WS_2 and $e_T^* = 0.30$ for IF-WS_2 at 300 K [39]. Thus, IF-WS_2 has approximately two thirds the intralayer charge as 2H-WS_2. This approximate 1.5:1 charge difference is replicated in the local charge numbers, with e_l^* decreasing proportionally in the IF compound. The intralayer charge differences summarized in Table II can be traced to differences in the LO-TO splitting and oscillator strength of the E_{2u} mode in 2H- and IF-WS_2. As already mentioned, these changes are easily observed in the spectral data (Fig. 3). The results imply that there is in fact a significant difference in the local environment and chemical bonding between the 2H- and IF- materials and that nanoparticle curvature changes the charging environment within the plane. A blocked "rigid layer" E_{2g} Raman mode is also consistent with these observations [25].

In the interlayer direction, the charge trend as characterized by the behavior of the A_{2u} mode is different (Table II). At 300 K, $e_T^* = 0.16$ for IF-WS_2 compared with $e_T^* = 0.15$ for 2H-WS_2. That e_T^* is larger in IF-WS_2 is indicative of slightly stronger interlayer interaction and enhanced charge environment in the curved nanoparticles compared with the bulk. As expected, the total effective charge within the layer (e_T^* from the E_{1u} mode) is always larger than that between layers (e_T^* from the A_{2u} mode), indicating that the majority of charge resides within the metal dichalcogenide layer in both materials.

Table II also displays the total and local effective charge of 2H- and IF-WS_2 at low temperature. Although the exact values of total and local effective charge differ slightly from their 300 K values (for instance, the total charge extracted from analysis of the xy-polarized E_{1u} mode of 2H-WS_2 is 0.51 at 10 K and 0.45 at 300 K), the overall trends between the layered and nanomaterial remain similar to those discussed above. Macroscopic effective charge within the layer decreases from 0.51 in the bulk to 0.34 in the nanomaterial (again, an approximate 1.5:1 charge difference), and local charge makes up approximately 50% of the total charge. The total charge extracted from the interlayer A_{2u} mode is slightly larger in the 2H material than in the IF nanoparticles at low temperature.

B. Curvature-Induced Local Symmetry Breaking in IF-WS_2

Are there other manifestations of curvature in the nanoparticles besides the aformentioned total and local effective charge differences? Certainly, strain and confinement have been of recent interest in both vanadium oxide inorganic nanotubes and silicon nanowires [41, 42]. In both cases, strain broadens the vibrational modes. Another effect of curvature is that the local, short range symmetry is formally lower than (and a subgroup of) the unstrained bulk. The reduction of local symmetry can change the selection rules, allowing formerly "infrared-silent" modes to become infrared active [43, 44]. Further, the curvature of each metal dichalcogenide layer within the nanoparticle is not uniform. This inhomogeneous structure also results in mode dispersion. Evidence for these effects, while present in the 300 K spectrum of IF-WS_2 (Fig. 3), is best illustrated in the low temperature spectral response.

Figure 5 displays the optical conductivity, $\sigma_1(\omega)$, of 2H- and IF-WS_2 at 10 K [34]. The low temperature spectral response of both materials is still dominated by the E_{1u} and A_{2u} modes, although because of the additional fine structure, the nanoparticle response is clearly much richer and more complicated than that of the bulk material. We attribute the additional vibrational structure to the formally "silent" and combination modes, activated (and dispersed) in the spectrum of IF-WS_2 by the symmetry breaking that results from the curved cage structure. For instance, some Raman modes are well-known conjugates of infrared active features [45]. The E_{2g}^1 and E_{1u}^2 conjugate pair is an example. The symmetry analysis and vector displacement diagrams of Verble and Wieting [14] (see also Table A.1, Appendix) also provide several candidates for silent mode activation, stating that the inactive B_{1g}, B_{2u}, and E_{2u} modes are nearly degenerate with several Raman- and infrared-active modes. Thus, the optical conductivity of IF-WS_2 likely contains weak contributions from all of these first-order structures, along with a substantial number of peaks that originate

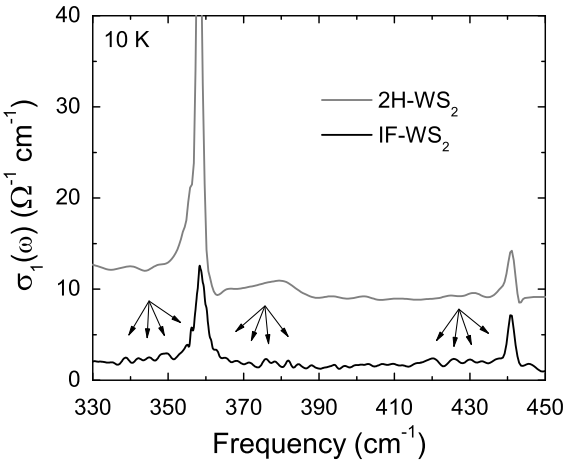


FIG. 5: Optical conductivity of 2H- and IF-WS_2 at 10 K. Arrows highlight the low-temperature symmetry breaking in the IF material. Ref. [46] lists the frequencies of these features. All of these small modes are reproducible, although it should be noted that the exact details of this fine structure will likely depend on particle size and distribution within a sample, the number of nanoparticle layers, and the nature of the defects.

from mode combinations and disorder effects.

Group theory can also be used to investigate possible second order infrared active combinations. When a direct product of two fundamental modes contains A_{2u} or E_{1u} symmetry in its character, it follows that a combination of those two modes will be infrared active. For example, $E_{1u} \bigotimes E_{2g} = B_{1u} + B_{2u} + E_{1u}$, and $A_{2u} \bigotimes E_{1g} = E_{1u}$. These combinations are both infrared active because their reducible representation contains E_{1u}. (Taking the direct product of this state with the x, y, and z dipole moment operators clearly contains the totally symmetric group.) Similarly, the sum and difference of other fundamental vibrational frequencies can lead to various infrared active combinations like $A_{2u} \bigotimes A_{1g}$, $E_{1u} \bigotimes A_{1g}$, $E_{1u} \bigotimes E_{1g}$, $B_{2u} \bigotimes E_{2g}$ and $B_{2u} \bigotimes B_{1g}$. We note that the longitudinal acoustic mode is intimately and extensively involved with many combination modes that appear in resonance Raman [23] and may be involved in the infrared-active combination modes of IF-WS_2 as well.

IV. CONCLUSION

We report the infrared vibrational properties of bulk and nanoparticle WS_2 in order to investigate the structure-property relations in these novel materials. In addition to the symmetry-breaking effects of local strain, nanoparticle curvature modifies the well-known charge environment of the bulk material. Using the E_{1u} mode as a local probe of charge behavior within the layer, we find an approximate 1.5:1 intralayer charge difference between the 2H- and IF- materials. The trend is different in the interlayer direction (probed by the A_{2u} mode) at 300 K. Here, effective charge increases slightly in the IF material compared to that in the bulk. We attribute the stronger interlayer interaction to nanoparticle curvature. Elucidating the relationship between structure and effective total and local charge in 2H- and IF-WS_2 is only the first step in understanding the fundamental interactions underlying the phenomenal mechanical and solid state lubricating properties of nanoscale metal dichalcogenides. Tuning MX_2 bond covalency may, for instance, allow simultaneous exploration of macroscopic mechanical properties, the charge environment, and potential surface effects.

V. ACKNOWLEDGEMENTS

Work at the University of Tennessee is supported by the Materials Science Division, Office of Basic Energy Sciences at the U.S. Department of Energy under Grant No. (DE-FG02-01ER45885). Work at the Weizmann Institute of Science is supported by the Helen and Martin Kimmel Center for Nanoscale Science and by NanoMaterials, Ltd. R.T. is the holder of the Drake Family Chair in Nanotechnology. We thank Albert Migliori and David Tománek for interesting discussions and Ronit Popovitz-Biro for the transmission electron microscope images.

APPENDIX: Group Theoretical Results for 2H-WS_2

In 1970, Verble and Wieting carried out a complete symmetry analysis on hexagonal layered compounds with the goal of analyzing vibrational mode symmetries. Our analysis differs from that in Ref. [14] in two ways: (1) a C_2'' correlation table accounts for the D_{3h} 2(c) site symmetry of tungsten, and (2) a σ_d correlation table accounts for the C_{3v} 4(f) site symmetry of sulfur [13, 47]. In Ref. [47] refer to Table 14, p. 50, and D_{6h} correlation table, p. 210. Table A.1 summarizes our results. Local strain in the IF-WS_2 breaks the selection rules of the 2H- "parent compound", as detailed in the text.

TABLE A.1:
Group Theoretical Analysis for 2H-WS_2

Atom	Site Symmetry		Irreducible Representation
W	D_{3h}	2(c)	$A_{2u} + B_{1g} + E_{2g} + E_{1u}$
S	C_{3v}	4(f)	$A_{1g} + A_{2u} + B_{1g} + B_{2u}$ $+ E_{1g} + E_{1u} + E_{2g} + E_{2u}$
Γ_{Total}			$2A_{2u} + 2B_{1g} + A_{1g} + B_{2u}$ $+ E_{1g} + 2E_{2g} + 2E_{1u} + E_{2u}$
$\Gamma_{Inactive}$			$2B_{1g} + B_{2u} + E_{2u}$
$\Gamma_{Acoustical}$			$A_{2u} + E_{1u}$
Γ_{Raman}			$2E_{2g} + A_{1g} + E_{1g}$
$\Gamma_{Infrared}$			$A_{2u} + E_{1u}$

[1] R. Tenne, L. Margulis, M. Genut, and G. Hodes, Nature **360**, 444 (1992).

[2] L. Margulis, G. Salitra, and R. Tenne, Nature **365**, 113 (1993).

[3] P.A. Parilla, A.C. Dillon, K.M. Jones, G. Riker, D.L. Schulz, D.S. Ginley, and M.J. Heben, Nature **397**, 114 (1999).

[4] L. Rapoport, Yu. Bilik, Y. Feldman, M. Homyonfer, S.R. Cohen, and R. Tenne, Nature **387**, 791 (1997).

[5] L. Rapoport, Y. Feldman, M. Homyonfer, H. Cohen, J. Sloan, J.L. Hutchison, and R. Tenne, Wear **225**, 975 (1999).

[6] L. Rapoport, N. Fleischer, and R. Tenne, Adv. Mater. **15**, 651 (2003).

[7] W.X. Chen, J.P. Tu, Z.D. Xu, R. Tenne, R. Rosentsveig, W.L. Chen, and H.Y. Gan, Adv. Eng. Mater. **4**, 686 (2002).

[8] C. Schuffenhauer, G. Wildermuth, J. Felsche, and R. Tenne, Phys. Chem. Chem. Phys. **6**, 3991 (2004).

[9] L. Rapoport, N. Fleischer, and R. Tenne, J. Mater. Chem. **15**, 1782 (2005).

[10] Y.Q. Zhu, T. Sekine, Y.H. Li, W.X. Wang, M.W. Fay, H. Edwards, P.D. Brown, N. Fleischer, and R. Tenne, Adv. Mater. **17**, 1500 (2005).

[11] Here, 2H is based on Ramsdell notation with 2 indicating the number of S-W-S slabs within the unit cell and H representing the lattice type (hexagonal).

[12] J.A. Wilson and A.D. Yoffe, Adv. Phys. **18**, 193 (1969).

[13] W.J. Schutte, J.L. De Boer, and F. Jellinek, J. Solid State Chem. **70**, 207 (1987).

[14] J.L. Verble and T.J. Wieting, Phys. Rev. Lett. **25**, 362 (1970).

[15] S. Uchida and S. Tanaka, J. Phys. Soc. Jpn. **45**, 153 (1978).

[16] G. Lucovsky, R.M. White, J.A. Benda, and J.F. Revelli, Pys. Rev. B **7**, 3859 (1973).

[17] G. Lucovsky, R.M. Martin, and E. Burstein, Phys. Rev. B **4**, 1367 (1971).

[18] G. Lucovsky, J.C Mikkelsen, Jr., W.Y. Liang, R.M. White and R.M. Martin, Phys. Rev. B **14**, 1663 (1976).

[19] E. Burstein, A. Pinczuk, and R.F. Wallis, in *Proceedings of the Conference on the Physics of Semimetals and Narrow-gap Semiconductors* (Pergamon Press, New York, 1971), p. 251.

[20] Y. Feldman, E. Wasserman, D. J. Srolovitz, and R. Tenne, Science **267**, 222 (1995).

[21] Y. Feldman, G.L. Frey, M. Homyonfer, V. Lyakhovitskaya, L. Margulis, H. Cohen, G. Hodes, J.L. Hutchison, and R. Tenne, J. Am. Chem. Soc. **118**, 5362 (1996).

[22] D.J. Srolovitz, S.A. Safran, M. Homyonfer, and R. Tenne, Phys. Rev. Lett. **74**, 1779 (1995).

[23] C. Sourisseau, F. Cruege, and M. Fouassier, Chem. Phys. **150**, 281 (1991).

[24] G.L. Frey, R. Tenne, M.J. Matthews, M.S. Dresselhaus, and G. Dresselhaus, J. Mater. Res. **13**, 2412 (1998).

[25] Unpublished data, P.C. Klipstein, Department of Physics, Clarendon Laboratory, University of Oxford, Oxford, England.

[26] G.L. Frey, S. Elani, M. Homyonfer, Y. Feldman, and R. Tenne, Phys. Rev. B **57**, 6666 (1998).

[27] M. Hershfinkel, L.A. Gheber, V. Volterra, J.L. Hutchison, L. Margulis, and R. Tenne, J. Am. Chem. Soc. **116**, 1914 (1994).

[28] M. Homyonfer, B. Alperson, Y. Rosenberg, L. Sapir, S.R. Cohen, G. Hodes, and R. Tenne, J. Am. Chem. Soc. **119**, 2693 (1997).

[29] Y. Feldman, A. Zak, R. Popovitz-Biro, and R. Tenne, Solid State Sci. **2**, 663 (2000).

[30] R. Rosentsveig, A. Margolin, Y. Feldman, R. Popoviz-Biro, and R. Tenne, Chem. Mater. **14**, 471 (2002).

[31] A. Margolin, R. Rosentsveig, A. Albu-Yaron, R. Popoviz-Biro, and R. Tenne, J. Mater. Chem. **14**, 617 (2004).

[32] R. Tenne, Angew. Chem. Int. Ed. **42**, 5124 (2003).

[33] F. Wooten, *Optical Properties of Solids* (Academic Press, New York, 1972).

[34] These optical constants include the real and imaginary parts of the dielectric function, $\epsilon_1(\omega)$ and $\epsilon_2(\omega)$, the energy loss function, $-\mathrm{Im}(1/\epsilon(\omega))$, and the optical conductivity, $\sigma_1(\omega)$. In our analysis, the low frequency data was extrapolated as a constant, and the high frequency data was extrapolated with an exponent of 2.4.

[35] In the optical conductivity, $\sigma_1(\omega)$, these features are centered at 356.5 and 438.3 cm^{-1} for the 2H compound and at 357.0 and 439.0 cm^{-1} for the IF nanoparticles.

[36] G. Herzberg, *Infrared and Raman Spectra of Polyatomic Molecules* (D. Van Nostrand Company, Inc., New York, 1945).

[37] H. Müeller, Phys. Rev. **50**, 547 (1936).

[38] F. Gervais, *Infrared and Millimeter Waves*, Vol. 8 (Academic Press, New York, 1983).

[39] We note that Uchida and Tanaka [15] report $e_T^* = 1.5$ and $e_l^* = 0.4$ for 2H-WS_2, emphasizing the difference between powder and single crystal measurements.

[40] e_l^* cannot be obtained for the z-polarized interlayer A_{2u} mode. The model for localized charge is developed for studying only the intralayer E_{1u} mode in the layered 2H bulk material [15, 19]. Since the Lorentz factor is negative for the A_{2u} mode, no realistic charge values could be determined.

[41] J. Cao, J. Choi, J.L. Musfeldt, S. Lutta, and M.S. Whittingham, Chem. Mater. **16**, 731 (2004).

[42] K.W. Adu, H.R. Gutíerrez, U.J. Kim, G.U. Sumanasekera, and P.C. Eklund, Nano. Lett. **5**, 409 (2005).

[43] Formally, the local site symmetry of a curved sheet is C_1, and all A modes are active. But practically, the nanoparticle curvature is small, so it is useful to consider the additional spectral features as perturbations to the planar picture.

[44] I. Loa, C. Möschel, A. Reich, W. Assenmacher, K. Syassen, and M. Jansen, Phys. Status Solidi B **223**, 293 (2001).

[45] T. Sekine, T. Nakashizu, K. Toyoda, K. Uchinokura, and E. Matsuura, Solid State Commun. **35**, 371 (1980).

[46] Within the clusters centered at ∼347, 379, and 426 cm^{-1}, we observe vibrational fine structure at 338.7, 342.1, 345.0, 349.1, 355.09, 356.2; 362.6, 365.0, 368.1, 371.5, 376.0, 378.2, 381.9, 384.5, 388.0, 394.0, 396.8; and 420.4, 425.7, 430.1, 433.0 cm^{-1}, respectively.

[47] W.G. Fateley, F.R. Dollish, N.T. McDevitt, and F.F. Bentley, *Infrared and Raman Selection Rules for Molecular and Lattice Vibrations: The Correlation Method* (Wiley-Interscience, New York, 1972).